J Adv Ceram

Research Article

# Structural evolution and failure mechanisms of APS tantalate high-entropy ceramic coatings in response to thermal cycle up to 1500 °C

Jiankun Wang[1,2,3], Lin Chen[1,2,✉], Luyang Zhang[1,2], Hao Xu[1,2,3], Qinglin Zhou[1,2], Jing Feng[1,2,3,✉]

Cite this article: Wang J, Chen L, Zhang L, et al. *J Adv Ceram* 2026, **15**(4): 9221261. https://doi.org/10.26599/JAC.2026.9221261

**ABSTRACT:** Thermal barrier coatings (TBCs) with high working temperatures and long service life are indispensable for the hot-end components of gas turbines and aircraft engines. This work designs and verifies that tantalate high-entropy ceramic (HEC) coatings are excellent TBCs with working temperatures reaching 1500 °C. We reveal the structural evolution and failure mechanisms of tantalate HEC coatings synthesized via air plasma spraying (APS). After they are subjected to thermal shock at 1500 °C for 614 cycles, thermal fatigue at 1150 °C for 12,830 cycles, and annealing at 1100 °C for 384 h. The thermal stress caused by the temperature gradient, differences in thermal expansion coefficients (TECs), and mechanical properties between ceramic coatings and bond coat (BC) lead to the spalling of coatings during thermal shock, while the effects of BC oxidation are limited. In thermal fatigue, the accumulative thermal stress between BC and thermally grown oxides (TGO) is higher than the fracture resistance when the *h*/*R* ratio is higher than 0.32 (*h* and *R* are the TGO thickness and undulation radius, respectively), which mainly leads to the spalling of coatings. Additionally, the effects of coating sintering and stiffness are also considered, which lead to surficial spalling during the high-temperature service. Two different failure mechanisms are proposed based on their microstructural evolution, and synthesized tantalate HEC coatings can be used at temperatures up to 1500 °C, which further promotes the design and application of high-performance TBCs.

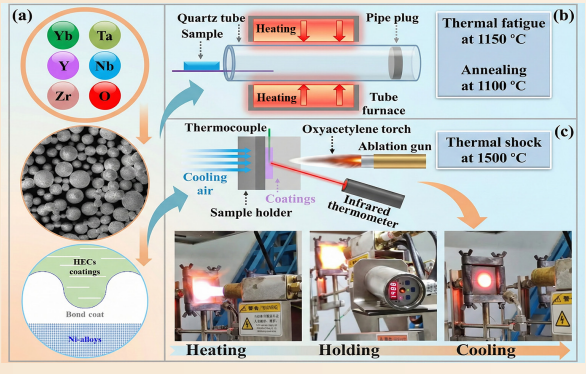


**KEYWORDS:** thermal barrier coatings (TBCs); high-entropy ceramic coatings; failure mechanisms; thermal cycle; thermal stress

## 1 Introduction

Next-generation oxide thermal barrier coatings (TBCs) are required to operate at temperatures beyond 1200 °C and are used to provide thermal insulation for alloy components [1–5]. To maintain excellent thermal insulation and long-term service, several characteristics are needed for TBCs. (i) The operating temperatures reach 1200–1500 °C, which are higher than those of yttria-stabilized zirconia (YSZ) [6]. (ii) A low thermal conductivity is needed, as the thermal insulation is inversely proportional to thermal conductivity [7–9]. (iii) High thermal expansion coefficients (TECs > $10\times10^{-6}$ $K^{-1}$, 1200 °C) reduce the thermal stress between TBCs and the bond coat (BC) because alloy BC usually has higher TECs ($(12–16)\times10^{-6}$ $K^{-1}$) than oxides [2,10]. (iv) A high fracture toughness ($K_{IC}$ > 3.0 MPa·$m^{1/2}$) is beneficial for inhibiting the formation and propagation of cracks during service [11–14]. Additionally, TBCs should have a high hardness to withstand the impacts of high-speed particles and a comparatively low modulus to increase their strain tolerance [12,13,15]. The current YSZ has several disadvantages. First, the phase transition leads to an operating temperature below 1200 °C, which is unstoppable [6,16]. Second, the thermal conductivity increases dramatically at high temperatures (> 900 °C) due to thermal radiation, and it will mitigate its thermal insulation [17,18]. Third, YSZ is severely corroded by CaO–MgO–$Al_2O_3$–$SiO_2$ (CMAS) melts, which leads to its premature failure [17]. Fourth, YSZ is corroded by moisture, and it is difficult to store and subsequently apply [19]. The problems of YSZ have been widely studied, but there are no effective ways to simultaneously overcome these deficiencies.

Various high-entropy ceramics (HECs) have been studied to boost properties to replace YSZ [20–22]. HECs mean that more than four elements are occupying one or more lattice sites and forming a single-phase material [23]. Four main effects exist in

[1] Faculty of Materials Science and Engineering, Kunming University of Science and Technology, Kunming 650093, China. [2] National-Local Joint Engineering Research Center for Technology of Advanced Metallic Solidification Forming and Equipment, Kunming 650093, China. [3] Southwest United Graduate School, Kunming 650092, China.

✉ Corresponding authors. E-mail: L. Chen, 1106846650@qq.com; J. Feng, jingfeng@kmust.edu.cn

Received: November 26, 2025; Revised: February 2, 2026; Accepted: February 8, 2026

HECs [21–24]: (i) The high-entropy effect improves stability; (ii) the sluggish diffusion effect mitigates the growth rate and inhibits the formation of second phases; (iii) the severe lattice distortion improves mechanical properties; and (iv) the cocktail effect produces unexpected properties. For example, $RETaO_4$ HECs have a low oxygen ionic conductivity and excellent high-temperature stability [25], and $RE_2Si_2O_7$ HECs have better CMAS corrosion resistance than their single-RE oxides [26]. Additionally, HECs of carbides [27], perovskite [28], tantalates [29], and composites [30] are widely studied to improve their performance for multifarious applications. There is no doubt that applications of HECs are effective in improving properties.

Based on the requirements of next-generation TBCs, we design and evaluate the service performance of novel tantalate HEC coatings at 1100–1500 °C, i.e., $Zr_{0.6}(YbYTaNb)_{0.1}O_2$, for the following reasons. Raghavan *et al.* [31] reported that $Y_2O_3$–$A_2O_5$ (A = Ta or Nb) costabilized $ZrO_2$ improves the high-temperature stability, which is used at 1000–1500 °C. Furthermore, $Y_2O_3$–$A_2O_5$ costabilized $ZrO_2$ has a thermal conductivity of 2.0 $W{\cdot}m^{-1}{\cdot}K^{-1}$ at 1000 °C, which is obviously lower than that of YSZ. Accordingly, $Zr_{0.6}(YbYTaNb)_{0.1}O_2$ tantalate HECs may have far better performance than YSZ. $Zr^{4+}$, $Yb^{3+}$, $Y^{3+}$, $Ta^{5+}$, and $Nb^{5+}$ cations have similar ionic radii, and $Yb^{3+}$, $Y^{3+}$, $Ta^{5+}$, and $Nb^{5+}$ cations enter the $ZrO_2$ lattice to form a single-phase oxide [32,33], which is instrumental in the formation of $Zr_{0.6}(YbYTaNb)_{0.1}O_2$ tantalate HECs. To validate the high-temperature performance and corresponding failure mechanisms of $Zr_{0.6}(YbYTaNb)_{0.1}O_2$ tantalate HECs, coatings are successfully synthesized via air plasma spraying (APS) technology. The failure mechanisms are analyzed from structural evolutions that experienced high-temperature measurements, including thermal shock at 1500 °C, thermal fatigue at 1150 °C, and annealing at 1100 °C. The above measurements are related to the thermal cycle performance of tantalate HEC coatings, and the changes in microstructures are vital points. This work elucidates the failure mechanisms of tantalate HEC coatings and proves that they are applied at temperatures up to 1500 °C.

## 2 Experiments and methods

### 2.1 Synthesis of coatings

The oxides were $ZrO_2$, $Ta_2O_5$, $Nb_2O_5$, $Y_2O_3$, and $Yb_2O_3$ from the Yihua mall (China) with a purity ≥ 99.9%. The powders were weighed according to the cationic ratio of $Zr_{0.6}(YbYTaNb)_{0.1}O_2$ and then ball milled within $C_2H_5OH$ for 20 h at 240 r/min. Subsequently, the mixtures were kept at 80 °C to evaporate $C_2H_5OH$ and then sintered at 1500 °C for 10 h to obtain the tantalate HEC powders. The spherical powders were further synthesized by Shaanxi Tianxuan Coating Technology Co., Ltd., China, using a spray granulation method. The coatings were sprayed on Ni-based alloy discs with a chamfer of 1.0 mm using an APS machine (SH-72k, Shenghua, China) as the parameters listed in Table 1, and the BC powders were $Ni_{46.37}Cr_{25.95}Co_{21.54}Al_{5.63}Y_{0.51}$ from Jinzhou Jinjiang Spraying Material Co., Ltd., China.

### 2.2 Identification of structures

Crystal structures were identified by an X-ray diffractometer (XRD; MiniFlex 600, Rigaku, Japan) when the microstructures and elemental contents were observed using a scanning electron microscope (SEM; EVO 180, Zeiss, Germany) equipped with an energy-dispersive spectrometer (EDS; Quantax 200, Bruker, Germany). The detailed interfacial structure was further identified by a transmission electron microscope (TEM; Tecnai G2 F20, FEI, USA), and the sample was cut by a focused ion beam (FIB; FEI Scios 2, Gatan, USA).

### 2.3 Measurements of mechanical properties

The hardness ($H$) and toughness ($K_{IC}$) were measured by a Vickers indentation device (HMV-G-FA, Shimadzu, Japan) under a load ($P$) of 0.2 kg. For each coating sample, six independent measurements were performed at different locations to ensure statistical reliability. The indentation morphology was recorded for subsequent crack length analysis. The $H$ and $K_{IC}$ were calculated according to Eqs. (1) and (2) [34, 35]:

$$H = 0.464\frac{P}{d^2} \tag{1}$$

$$K_{IC} = 0.016\sqrt{\frac{E}{H}}\cdot\frac{P}{c^{1.5}} \tag{2}$$

where $d$ is the length of the indentation diagonal; $c$ is the length of the cracks; $E$ is half of the Young's modulus ($E_{nano}$) measured via a nano-indentation device (iNano instrument, iMicro, USA). Bulk $NiCr_2O_4$ ceramics with the same composition as thermally grown oxides (TGO) were synthesized via solid-state reaction sintering. The elastic modulus ($E_{TGO}$) was measured using a nano-indentation device, and Poisson's ratio ($\upsilon_{TGO}$) was determined using an ultrasonic pulser/receiver equipment (UMS-100, TECLAB, France) [7,11].

### 2.4 Measurements of service performance

During the one-time thermal shock measurement, the coatings were heated to 1500 °C within 20 s by the acetylene flame, and the holding time was 20 s, which were then cooled by compressed air for 20 s. The thermal fatigue was conducted at 1150 °C, which had a holding time of 5 min, and then the coatings were cooled in air for 5 min. To study the changes in microstructures, the coatings were isothermally oxidized at 1100 °C for 384 h in an air atmosphere using a muffle furnace. During these measurements, the tantalate HEC coatings were treated as a failure when the spalling area was higher than 20%. The TGO thickness was measured using SEM. For each sample, cross-sectional images were obtained at multiple representative locations along the coating–substrate interface. Within each field of view, five separate measurements were taken at different positions to ensure statistical reliability. The TGO thickness at each measurement point was determined by measuring the perpendicular distance from the bond coat surface to the outer boundary of the oxide layer. The five measurements from each location were then averaged to obtain the mean TGO thickness value for that specific region.

**Table 1** Synthesis parameters of tantalate HEC coatings and BC during APS, including plasma power (PP (kW)), plasma arc electric current (PAEC (A)), plasma arc voltage (PAV (V)), gas flow rate (GFR ($NL{\cdot}min^{-1}$), feeding rate of powders (FRP ($g{\cdot}min^{-1}$)), spraying speed (SS ($mm{\cdot}s^{-1}$)), and spraying distance (SD (mm))

| Coating | PP (kW) | PAEC (A) | PAV (V) | GFR ($NL{\cdot}min^{-1}$) | | FRP ($g{\cdot}min^{-1}$) | SS ($mm{\cdot}s^{-1}$) | SD (mm) |
|---|---|---|---|---|---|---|---|---|
| | | | | Ar | $H_2$ | | | |
| Tantalate HECs | 45 | 557 | 80.8 | 40 | 9.6 | 25 | 46 | 180 |
| BC | 38 | 523 | 72.6 | 45 | 8.4 | 28 | 46 | 200 |

## 3 Results

### 3.1 Microstructures and crystals of spherical powders

Figure 1(a) shows that most spherical powders have diameters of 20–80 μm. Each element is uniformly distributed, and the EDS spectra are shown in Fig. 1(b). Figure 1(c) presents the particle size distribution analysis, The particle size of the powder ranges from 25–75 μm, with a mean particle size of 42.9±9.7 μm. These particle size characteristics and the high sphericity of the powders indicate that the feedstock material is well suited for APS. Figure 1(d) shows that the as-sintered powders are crystallized in the tetragonal $YTaO_4$ (*T*-$YTaO_4$) and tetragonal YSZ (*t*-YSZ) phases. Minor contents of monoclinic YSZ (*m*-YSZ) are found, while they are not detected in the synthesized coatings below.

Based on the $Y_{0.5}Ta_{0.5}O_2$–$ZrO_2$ and $YO_{1.5}$–$TaO_{2.5}$–$ZrO_2$ phase diagrams, the crystal structures change with temperature and composition [32,36]. The solid solution degree of $ZrO_2$ in $Y_{0.5}Ta_{0.5}O_2$ is less than 28 mol%, while the solid solution degree of $Y_{0.5}Ta_{0.5}O_2$ in $ZrO_2$ is less than 35 mol%. The high-entropy effects lead to high-temperature *T*-$YTaO_4$ being stable at room temperature, and *t*-$ZrO_2$ is stabilized by $Yb_2O_3$–$Y_2O_3$–$Ta_2O_5$–$Nb_2O_5$ [32,36,37]. However, $Yb^{3+}$, $Y^{3+}$, $Ta^{5+}$, and $Nb^{5+}$ completely enter the $ZrO_2$ lattice to form fluorite ceramic coatings during APS, as proven below. The temperatures during APS are far higher than the melting points of tantalate and zirconium oxides, which promote the formation of single-phase tantalate HEC coatings. Thus, the crystal structures of spherical powders do not severely affect the following measurements and analysis.

### 3.2 Microstructures of tantalate HEC coatings

Figure 2(a) shows the tantalate HEC coatings with a thickness of approximately 150 μm and BC with a thickness of approximately 120 μm. Additionally, Fig. 2(b) shows the synthesized coatings in the vicinity of the chamfers of the substrates. A chamfer is used to reduce thermal stress between the coatings and substrates, which will avoid the premature failure of coatings due to enormous thermal stress on the edge. Surface roughness measurements reveal that the as-sprayed tantalate HEC coatings exhibit an average surface roughness of 9.64±2.82 μm over a 1 mm × 1 mm area and 9.48±0.87 μm over a 10 mm × 10 mm area, indicating good surface uniformity across different measurement scales (Fig. S1 in the Electronic Supplementary Material (ESM)). Figure 2(c) shows that tantalate HEC coatings and BC are clearly distinguished based on the EDS mapping of Zr, Y, and Nb. Furthermore, minor $Al_2O_3$ is produced during APS according to Al and O segregations in BC.

The components of tantalate HECs and BC are further identified by EDS and are shown in Fig. 3. The as-sprayed tantalate HEC coatings are crystallized into a fluorite phase, as shown in Fig. 4, and the specific content of each element is shown in Fig. 3(b). Additionally, a Y/Ta-rich phase is found, which is too tiny to be counted. For BC, the Cr and Ni segregations are found at the interface, which is marked by a blue point. Figure 3(d) indicates that the Cr and Ni segregation areas are oxidized to form TGO during APS, and the elemental contents of most areas in BC are consistent with the raw alloy powders shown in Fig. 3(e). The oxidized area is further confirmed as $NiCr_2O_4$ based on the following TEM and EDS results.

The as-sprayed tantalate HEC coatings are crystallized into a fluorite phase, and $Yb^{3+}$, $Y^{3+}$, $Ta^{5+}$, and $Nb^{5+}$ cations enter the $ZrO_2$ lattice during APS. The $YO_{1.5}$–$ZrO_2$ phase diagram shows that the solid solution degree of $YO_{1.5}$ in $ZrO_2$ is as high as 50 mol%, which is beneficial for the formation of fluorite tantalate HEC coatings [32,37,38]. A minute second phase is found in the tantalate HEC coatings, which is omitted. The oxidation of BC is inevitable during APS due to the high temperatures and air environments. It is clear that the tantalate HEC coatings and BC are successfully synthesized via APS on the surface of Ni-based alloys, and they are used for thermal measurements.

### 3.3 Thermal shock at 1500 °C

Figure 5(a) shows the cross-sectional microstructures of tantalate HEC coatings after 460 thermal shock measurements at 1500 °C, and some coatings are spalled at the center. Additionally, obvious transverse cracks are observed at the interface between the

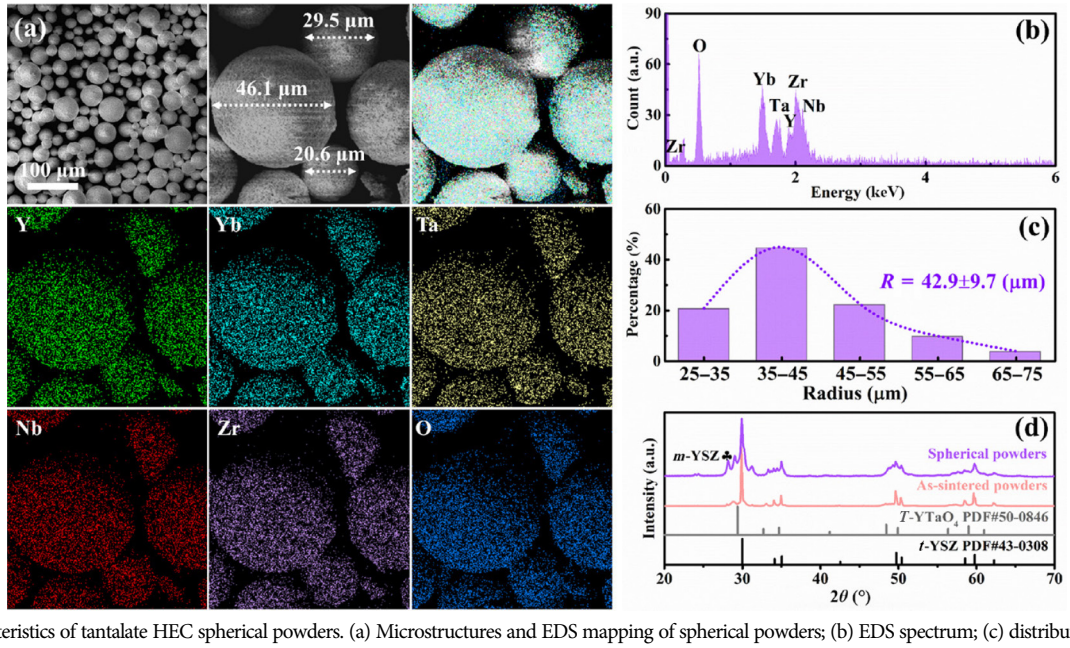


**Fig. 1** Characteristics of tantalate HEC spherical powders. (a) Microstructures and EDS mapping of spherical powders; (b) EDS spectrum; (c) distributions of powder diameters; (d) XRD patterns. Spherical powders of tantalate HECs are synthesized via spray granulation. Each element is uniformly distributed on spherical powders, and they have a mean diameter of 42.9±9.7 μm, which can be used to synthesize coatings via APS technology.

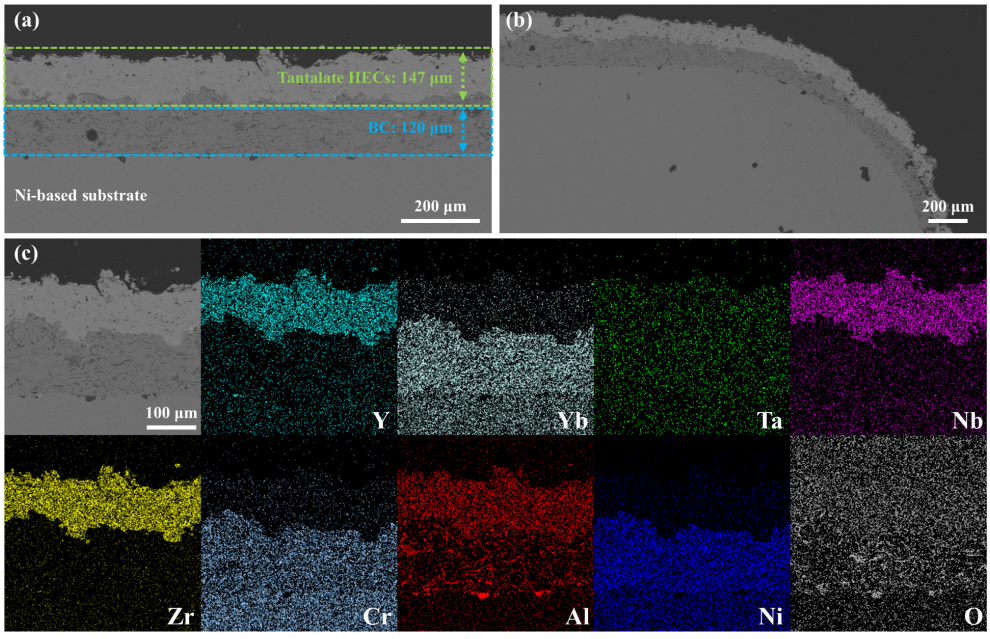


**Fig. 2** Cross-sectional microstructures of as-sprayed tantalate HEC coatings. (a) Thickness of tantalate coatings and BC; (b) coatings and BC at edge; (c) EDS mapping. As-sprayed tantalate coatings are approximately 150 μm when BC is 120 μm, and minor alloys are oxidized during APS process.

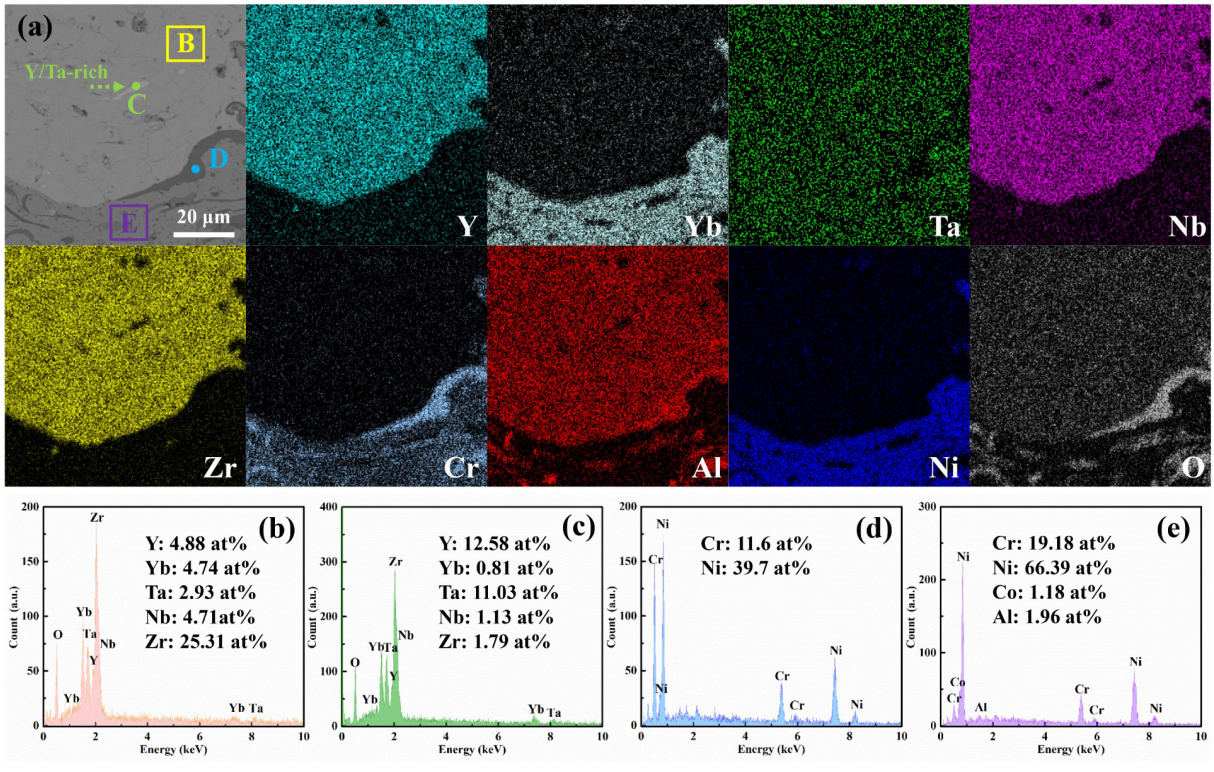


**Fig. 3** Interface between tantalate coatings and BC. (a) Micromorphology and distributions of each element; (b–e) elemental contents obtained from EDS of points B–E marked in (a), respectively. Y/Ta segregation is found in as-sprayed tantalate coatings.

ceramic coatings and BC caused by the interfacial thermal stress, as shown in Fig. 5(c). Figure 5(b) shows that abundant TGO is formed in BC, and numerous tiny transverse cracks are formed, which further grow and intersect to lead to the spalling of coatings. Some tiny longitudinal cracks are also found, and they are beneficial for reducing thermal stress [15,39,40]. Figure 5(d) shows that TGO mainly contains Cr, Ni, and O, and $NiCr_2O_4$ may be formed. After 460 measurements, the spalling area of the tantalate HEC coatings is less than 20%, and we continue the measurements up to 614, when the spalling area is higher than 20%.

Figure 6(a) shows that the residual tantalate HEC coatings are minor, and most BC is oxidized to form TGO, as shown in Fig. 6(b). The TGO mainly contains Cr, Ni, and O, as shown in Fig. 6(c), which is similar to the results shown in Fig. 5(d). Importantly, TGO is formed within the whole BC, while no continuous or dense TGO layer is formed on the surface of BC. No obvious cracks are detected within BC, and the failure of

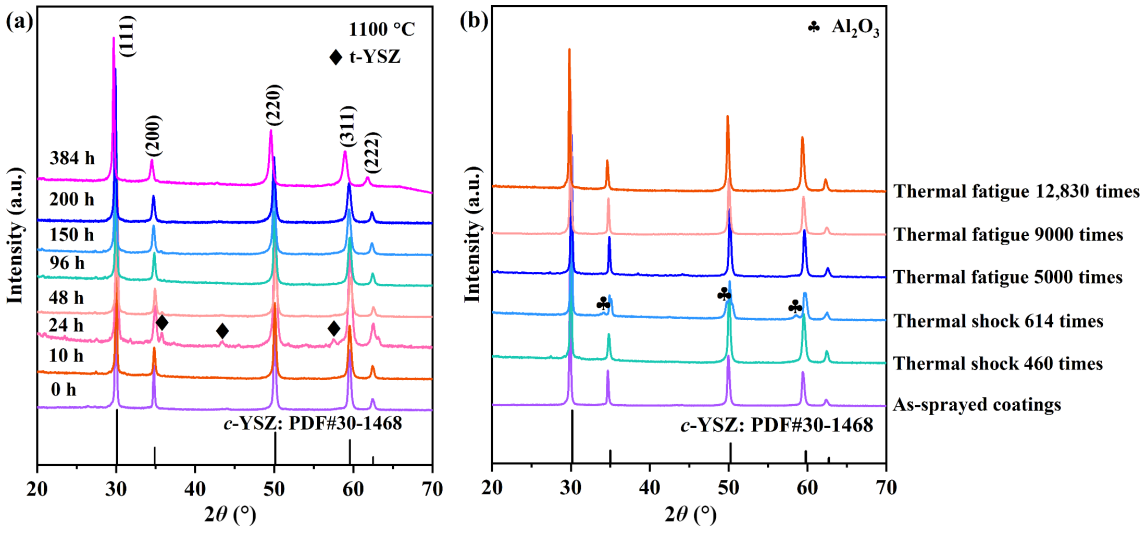


**Fig. 4** XRD patterns of tantalate HEC coatings after different measurements. (a) XRD patterns after holding at 1100 °C for 384 h; (b) XRD patterns after thermal fatigue and shock. Tantalate HEC coatings exhibit excellent high-temperature phase stability, and they maintain a cubic fluorite phase after various measurements.

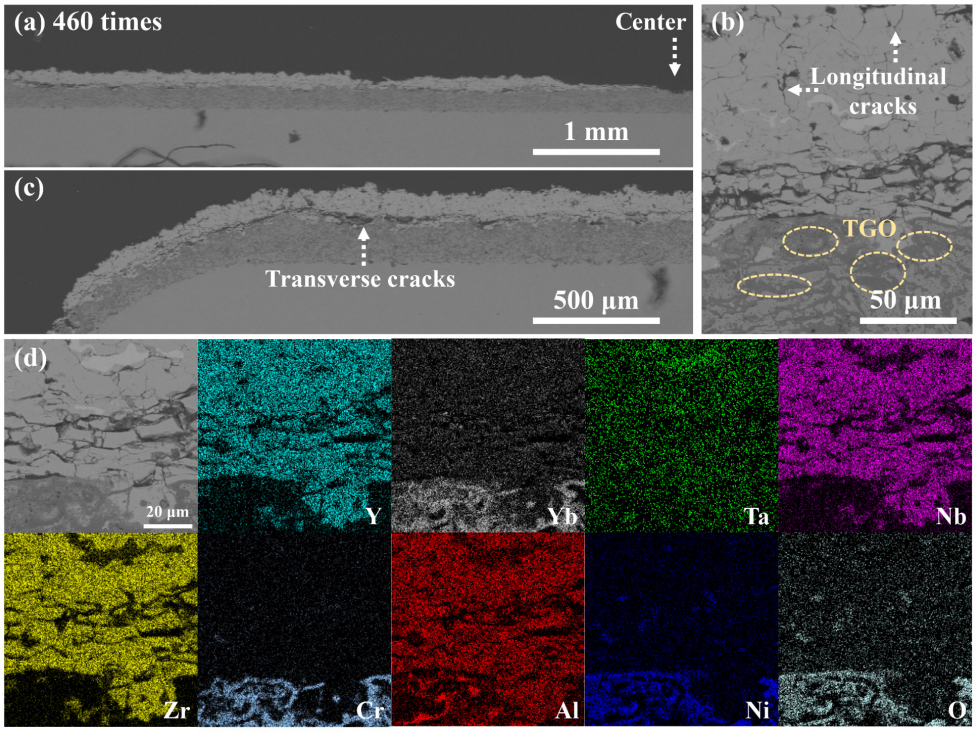


**Fig. 5** Structural evolution of tantalate HEC coatings and BC after 460 thermal shocks at 1500 °C. (a) Ceramic coatings around the center; (b) structural characteristics in ceramic coatings and BC; (c) ceramic coatings on edge; (d) elemental distributions obtained from EDS mapping. Minor spalling is detected at center, and obvious transverse cracks are found between ceramic coatings and BC, while fine longitudinal cracks are found in tantalate coatings. TGO is produced in BC, which will lead to spalling of tantalate HEC coatings with further measurements.

tantalate HEC coatings is mainly affected by the transverse cracks between BC and tantalate HEC coatings. The failure mechanisms of tantalate HECs coatings observed in the present study differ distinctly from those reported in the literature, where cracks are generally found to form between TGO and BC due to thermal stress, and the subsequent linking of cracks at the TGO/BC interface with those in the ceramic coating ultimately leads to the spalling of TBCs [2,10,41], and they are further discussed below.

During thermal shock, the increasing, holding, and cooling time is 20 s, meaning that the temperature changes quickly. Therefore, the thermal stress between tantalate HEC coatings and BC is caused by the differences in TECs and modulus, as well as the undulation of BC [2,10,42]. The quick changes in temperature and comparatively short holding time at 1500 °C lead to the formation of no continuous or dense TGO layer on BC; accordingly, there are no cracks at the interface between TGO and BC. The thermal stress between tantalate HEC coatings and BC during thermal shock results in their failure.

### 3.4 Thermal fatigue at 1150 °C

The change in temperature during thermal fatigue at 1150 °C is much slower than that in thermal shock at 1500 °C, and measurements of thermal fatigue are as high as 12,830 cycles before failure. Figure 7(a1) shows that minor spalling is found on

the tantalate HEC coatings after 5000 thermal fatigue cycles, while no obvious transverse cracks are found. Figure 7(a2) and Fig. S2 in the ESM reveal that the oxidized area in BC is limited at this early stage. The TGO layer appears discontinuous and relatively thin, with an average thickness of approximately 2–3 μm. The EDS mapping in Fig. S2(c) in the ESM shows that TGO is enriched in Cr, Ni, and O, while the distribution is not yet continuous along the BC and ceramic coating interface. At this stage, the thin and discontinuous TGO does not generate sufficient thermal stress to initiate obvious cracks, and the coating system remains relatively intact.

Figure 7(b1) shows that the tantalate HEC coatings are still complete after 9000 thermal fatigue cycles; however, obvious transverse cracks are found between the BC and tantalate HEC

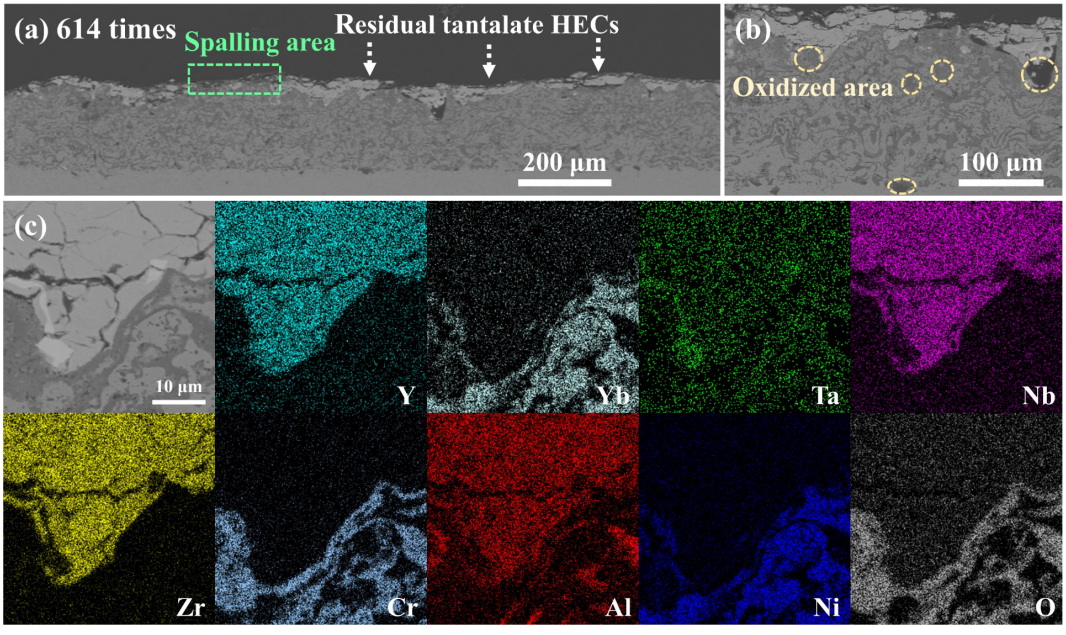


**Fig. 6** Structural evolution of tantalate HEC coatings and BC after 614 thermal shocks at 1500 °C, and peeling area of tantalate coatings is higher than 20%. (a) Residual tantalate HEC coatings; (b) oxidized area in BC; (c) elemental distributions obtained from EDS mapping. Tantalate HEC coatings fail after thermal shock at 1500 °C for 614 cycles, and residual tantalate HEC coatings are less than 50 μm on surface. BC is massively oxidized, and large-area TGO is found in vicinity of interface between BC and tantalate HEC coatings.

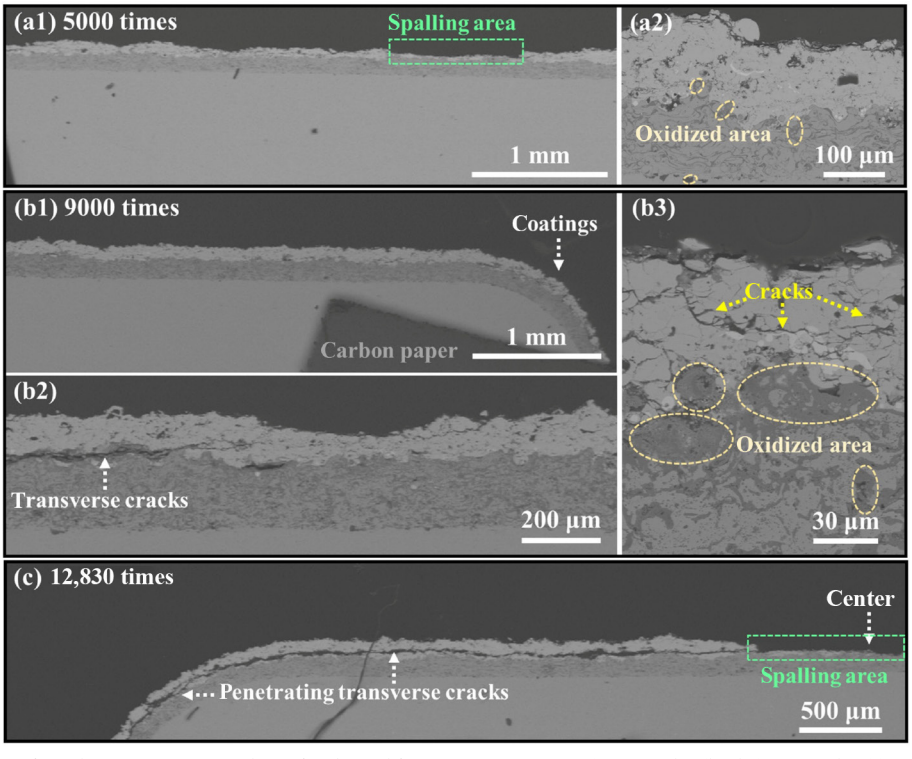


**Fig. 7** Structural evolution of tantalate HEC coatings and BC after thermal fatigue at 1150 °C. (a1, a2) 5000 cycles; (b1–b3) 9000 cycles; (c) 12,830 cycles. BC is oxidized with increasing holding time, and longitudinal and transverse cracks are produced in tantalate HEC coatings. After 12,830 thermal fatigue cycles, the tantalate HEC coatings fail when the spalling area is higher than 20%. A penetrating transverse crack is formed within coatings, and changes in cracks in ceramic coatings and oxidized area in BC prove that thermal stress between BC and ceramic coatings increases with increasing time.

coatings, as shown in Fig. 7(b2). Furthermore, Fig. 7(b3) shows that numerous tiny cracks are found within tantalate HEC coatings, and BC in the vicinity of ceramic coatings is obviously oxidized, indicating that thermal stress is significantly increased [43,44]. The detailed microstructural characterization in Fig. S3 in the ESM reveals that a continuous and dense TGO layer has been established at this stage, with the thickness increasing to 5–7 μm. The formation of a continuous TGO layer marks a critical transition point in the coating degradation process: Below this thickness, the TGO remains discontinuous, and the interfacial stress is insufficient to cause cracking; once the TGO becomes continuous with a thickness exceeding 5 μm, the accumulated thermal stress reaches a critical level to initiate transverse cracks at the ceramic coating and TGO interface. The EDS mapping in Fig. S3(d) in the ESM further confirms that the TGO composition remains predominantly Cr, Ni, and O, indicating a stable $NiCr_2O_4$ spinel structure. Figure 7(c) shows a penetrating transverse crack at the interface between the BC and tantalate HEC coatings, and evident spalling is found at the center of the sample, which indicates failure. The detailed TGO characterization in Fig. S4 in the ESM shows that the TGO thickness exceeds 10 μm after 12,830 thermal fatigue cycles. Due to the undulation morphology of the BC surface, the TGO thickness exhibits significant spatial variation: The TGO is relatively thinner at the undulation valleys (8–10 μm) and considerably thicker at the undulation peaks (15–20 μm). This nonuniform TGO distribution generates stress concentration at the undulation peaks, which promotes crack initiation and propagation along the ceramic coating and TGO interface. The EDS mapping in Fig. S4(b) in the ESM confirms that the TGO maintains the $NiCr_2O_4$ composition even after prolonged thermal fatigue exposure. Throughout the thermal fatigue process, the TGO layer is primarily composed of Cr, Ni, and O, as confirmed by the EDS mapping results in Figs. S2–S4 in the ESM. This indicates that the TGO is mainly $NiCr_2O_4$ spinel rather than α-$Al_2O_3$, which is typically formed as a protective oxide layer in conventional *M*CrAlY bond coats [41,45,46]. The preferential formation of $NiCr_2O_4$ over $Al_2O_3$ may be attributed to the specific thermal conditions during fatigue testing. The rapid heating (3 min) and cooling (2 min) cycles do not provide sufficient time for the selective oxidation of Al to establish a continuous $Al_2O_3$ layer and instead promote the oxidation of more readily available Ni and Cr elements at the BC surface. The $NiCr_2O_4$ spinel has a higher growth rate than α-$Al_2O_3$, which contributes to the relatively rapid TGO thickening observed in this study. Importantly, no obvious cracks are observed between TGO and BC throughout the thermal fatigue process, indicating that the TGO/BC interface maintains good adhesion and that failure initiates from the ceramic coating side rather than through TGO/BC delamination.

The microstructural evolutions after thermal fatigue at 1150 °C have something in common with those documented in Section 3.3, and thermal stress between BC and ceramic coatings is the main factor. The progressive thickening of TGO from the initial 2–3 μm to over 10 μm, combined with its nonuniform distribution along the undulated BC interface, contributes to the gradual accumulation of thermal stress at the ceramic coating/TGO interface. The enlargements and interlinks among numerous tiny cracks form penetrating transverse cracks and lead to spalling of the coatings. Based on the correlation between the TGO thickness evolution and crack initiation observed in this study, the critical TGO thickness for crack formation is determined to be approximately 5–7 μm in this tantalate HEC coating system, which is consistent with the critical TGO thickness range reported for conventional YSZ-based TBC systems.

### 3.5 Annealing at 1100 °C

The failure of tantalate HEC coatings is mainly caused by thermal stress between BC and ceramic coatings, and BC is oxidized to form $NiCr_2O_4$ TGO. Usually, the formation of TGO and increases in its thickness are connected to the heat treatment temperature and time. The thermal shock at 1500 °C displays quick changes in temperature, and its holding time is short. Therefore, there is no continuous or dense TGO layer. During thermal fatigue at 1150 °C, a thick TGO layer is formed after 9000 measurements, and both tiny cracks and obvious transverse cracks are observed in the ceramic coatings. Therefore, the inner thermal stress in ceramic coatings and interfacial thermal stress between BC and ceramic coatings synergistically contribute to failure. To further study the origins of these two types of thermal stress, the tantalate HEC coatings are kept at 1100 °C for 384 h, and the changes in crystal structures and microstructures are investigated.

Figure 8 shows microstructural evolutions of tantalate HEC coatings after holding at 1100 °C for 384 h, where cracks, pores, semimolten and unmolten particles are found. Obvious cracks and fine recrystallization grains are found on ceramic coatings after holding at 1100 °C for 150–384 h, and recrystallization will increase the inner thermal stress [47]. Additionally, Figs. 8(g1) and 8(h3) show the fragmented powders and coatings, and they are indicators of inner thermal stress. The increased inner thermal stress leads to fragmentation and gradual spalling of ceramic coatings, which are consistent with the microstructures shown in Figs. 5(a) and 7(a1). Figure 5(a) shows that tantalate HEC coatings maintain a fluorite structure after holding at 1100 °C for 384 h. Only minor contents of *t*-YSZ are found in coatings heat treated for 24 h. Figure S5 in the ESM shows that each element is distributed evenly, and no precipitated phase is found. Figure 5(b) shows that tantalate HEC coatings maintain a fluorite structure after thermal fatigue and thermal shock, and minor peaks of $Al_2O_3$ are found after thermal shock at 1500 °C for 614 cycles. The above results show that the as-sprayed coatings exhibit excellent high-temperature stability, and they can be used at temperatures up to 1500 °C.

The evolution of BC microstructures and thermal stress between BC and ceramic coatings are the main causes of coating spalling, and Fig. 9 shows the structural evolution of BC after holding at 1100 °C for 384 h. Inner oxidation is found in the as-sprayed BC, as marked in Fig. 9(a), and the interfacial oxidation marked by the green rectangle is triggered with increasing holding time. With increasing holding time, internal oxidation is further promoted, as marked by the red rectangle. When the holding time exceeds 48 h, interfacial oxidation interlinkage is found, and a dense, continuous TGO layer is formed, which will further become thicker with increasing holding time. Additionally, internal oxidation interlinkage is detected when the holding time is 96–384 h, and the thickness of the internal TGO is increased, as marked with a yellow rectangle. Figure 9(b) shows that Ni and O are gathered together at the interface TGO, while the internal TGO contains abundant Al. Accordingly, the compositions of TGO in Fig. 9 are different from the results in Figs. 5 and 6, and Figs. S2–S4 in the ESM, which may be caused by the different thermal measurements.

The formation of TGO and thermal stress between BC and tantalate HEC coatings are the main factors for spalling of ceramic coatings, while the effects of inner stress caused by sintering and recrystallization of ceramic coatings are also studied. The

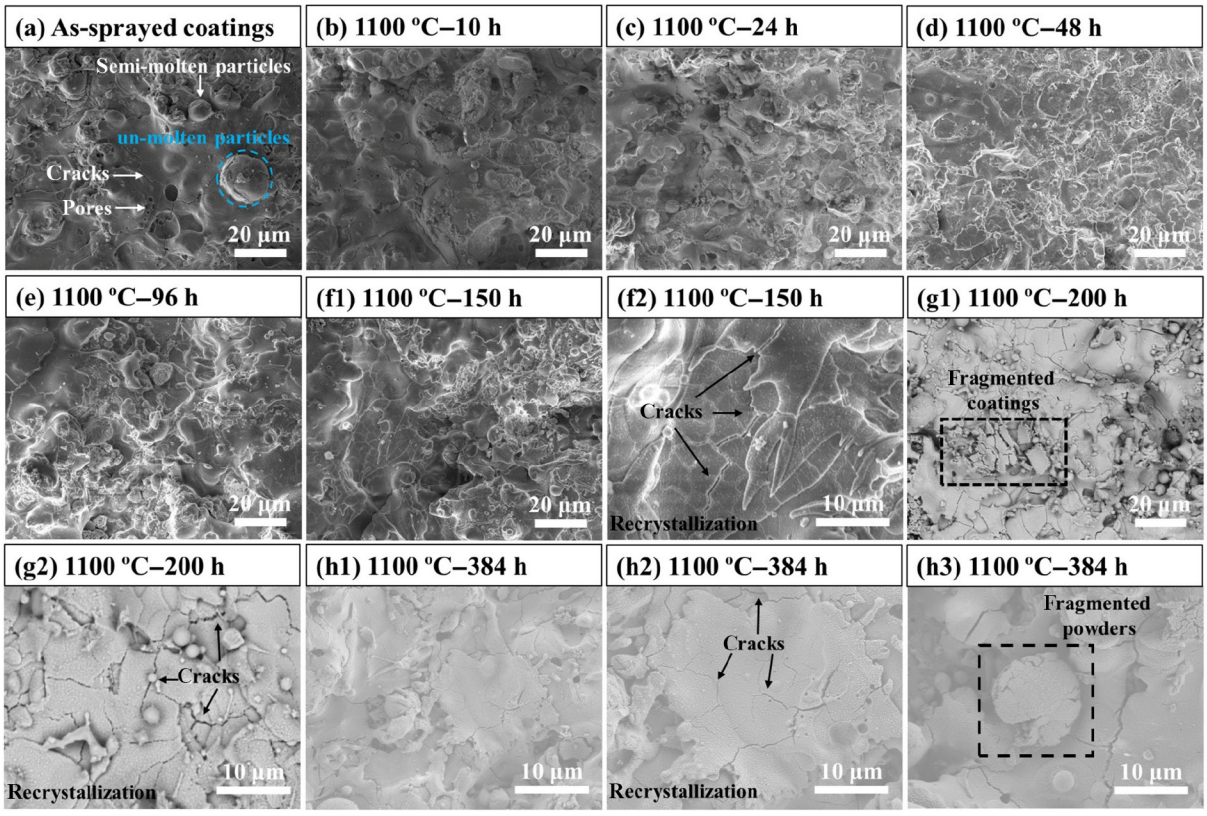


**Fig. 8** Structural evolution of tantalate HEC coatings after holding at 1100 °C for 384 h. (a–h) Surface microstructures after holding for 0, 10, 24, 48, 96, 150, 200, and 384 h, respectively. Semimolten and unmolten particles are found in as-sprayed coatings, and there is a small number of pores and cracks. Heat treatment at 1100 °C did not change crystal structures of tantalate HEC coatings. However, recrystallization is found in coatings when holding time is longer than 150 h, which causes cracks and destruction of coatings.

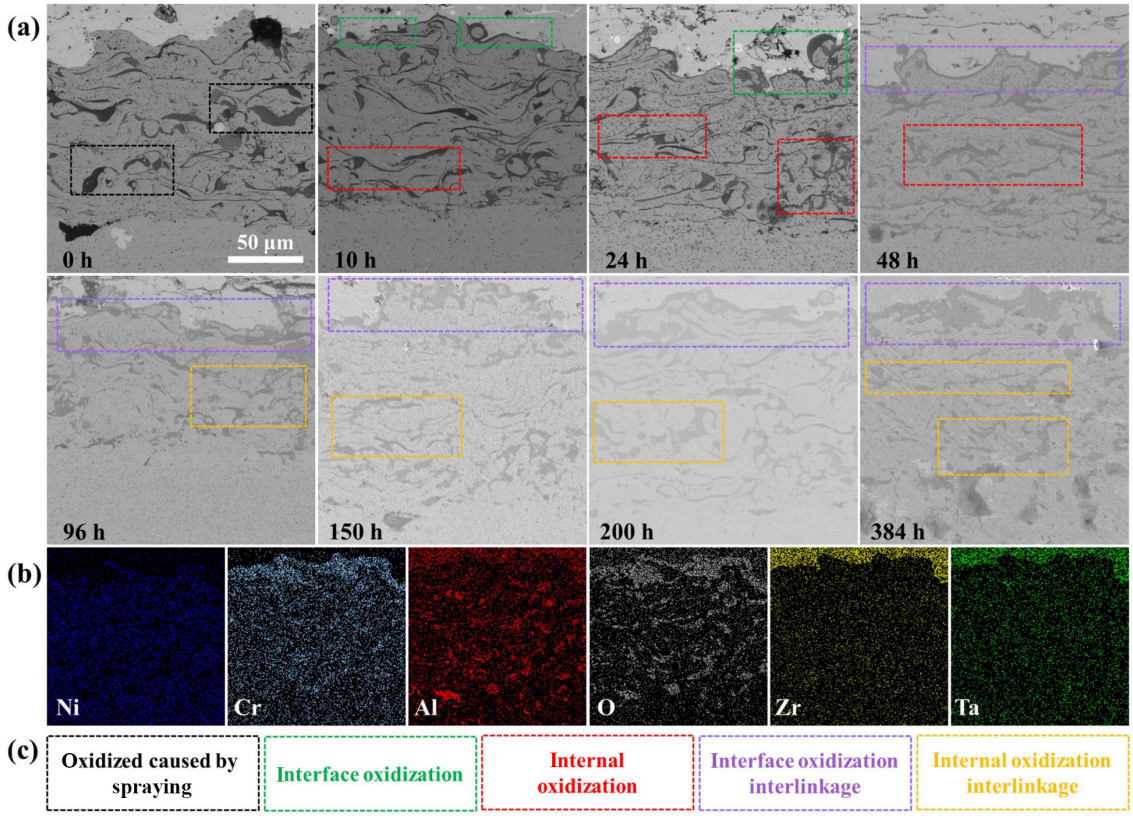


**Fig. 9** Structural evolution of BC after holding at 1100 °C for 384 h. (a) Structural characteristics; (b) EDS mapping after 384 h heat treatment; (c) meaning of dashed rectangles used in (a). BC is oxidized during APS process, and oxidized area increases with increasing holding time at 1100 °C.

evolutions of BC and TGO are different when the tantalate HEC coatings are subjected to different thermal measurements, but the intrinsic failure mechanisms are enormous thermal stresses between BC and ceramic coatings, and they are key points. In addition to the TGO composition and thickness, the oxidation rate is also considered. The three types of thermal measurements show that both interface and internal oxidation of BC are triggered, and the oxidation rates increase with increasing measurement time. Accordingly, the TGO thickness, thermal stress, and oxidation rates of BC are discussed in Section 4.

## 4 Discussion

### 4.1 Evolutions of TGO microstructures

Figure 10(a) shows the oxidation rate of BC after being kept at 1100 °C for 384 h, which increases as the holding time increases and reaches a maximum of 31.2% at 200 h. The microstructures used to calculate the oxidation rate are shown in Fig. 10(b). A dense and continuous TGO layer is formed on BC after holding at 1100 °C for 384 h, indicating that further internal oxidation of BC is difficult to realize, as the TGO will stop the migration of oxygen. The oxidation rate of BC after thermal shock at 1500 °C for 614 cycles is 38.4%, and it is 39.7% after thermal fatigue at 1150 °C for 12,830 cycles. The oxidation rates are similar when tantalate HEC coatings fail. No obvious cracks are found in BC and at the interface between BC and TGO, proving that the internal thermal stress is relatively low, which will not lead to the formation of penetrating cracks.

In addition to the oxidation area, the thickness of TGO is a main factor resulting in enormous thermal stress between BC and ceramic coatings. The thickness of TGO after thermal shock and thermal fatigue measurements is not clear, and we count the thickness of TGO after holding at 1100 °C for 384 h. Figure 10(a) shows that the average TGO thickness increases quickly with increasing holding time, and an approximate linear relationship is found. The observed approximate linear relationship between TGO thickness and heat treatment time deviates from the classical Wagner oxidation theory, which predicts a parabolic growth law ($\delta^2 \propto t$, where $\delta$ is the oxide thickness, and $t$ is the oxidation time) for diffusion-controlled oxidation processes [48,49]. In this study, the TGO thickness increases from approximately 2.1 μm at 10 h to 8.1 μm at 200 h and reaches over 15 μm at 384 h, exhibiting an average growth rate of approximately 0.04 μm/h. This near-linear behavior can be attributed to several factors. First, the TGO formed here is primarily $NiCr_2O_4$ spinel rather than α-$Al_2O_3$. The growth rate of $NiCr_2O_4$ spinel is typically 2–5 times faster than that of α-$Al_2O_3$ due to the concurrent diffusion of multiple cation species ($Ni^{2+}$ and $Cr^{3+}$), which sustains a near-linear growth rate within the investigated time range [50,51]. Second, the porous microstructure of the APS-deposited coatings provides abundant fast diffusion paths for oxygen transport, maintaining an enhanced oxidation rate that deviates from the typical parabolic kinetics observed in dense coating systems. Furthermore, the simultaneous occurrence of interfacial and internal oxidation within BC, as evidenced by the oxidation rate reaching 31.2% at 200 h (Fig. 10), complicates the overall oxidation kinetics. Similar near-linear TGO growth behaviors have been reported in other APS–TBC systems where complex microstructure and multiphase oxidation processes lead to nonclassical growth kinetics [52,53]. Figure S6 in the ESM shows the typical TGO structures, and the largest TGO thickness is higher than 30 μm, which exceeds the critical thickness of TGO [45,47,54,55].

The relevant thermal stress is comparatively low during the isothermal heat treatment. The top coat (TC, i.e., tantalate HEC coatings), TGO, and BC are distinguished by EDS mapping, as shown in Fig. 11(a), and Table 2 lists the detailed components of P2 and P3, which correspond to TGO and TC, respectively. Figure 11(b) shows that TGO marked as P2 has a fluorite structure corresponding to $NiCr_2O_4$, proving that TGO is $NiCr_2O_4$, which is also reported in other studies [56,57].

### 4.2 Evolutions of mechanical properties

During the isothermal heat treatment at 1100 °C, the thermal stress is relatively low based on the evolution of TGO and BC, while the thermal stress during thermal fatigue and shock is much higher due to the misfits in TECs and mechanical properties among TC, TGO, and BC [58]. The hardness and modulus of tantalate HEC coatings increase with increasing holding time at 1100 °C, caused by the sintering of ceramic coatings [47,59]. Figures 12(a) and 12(b) show that the nano Young's modulus and hardness of tantalate HEC coatings and BC increase with increasing holding time at 0–200 h, and they tend to be constant when the holding time is longer than 200 h. The cracks are

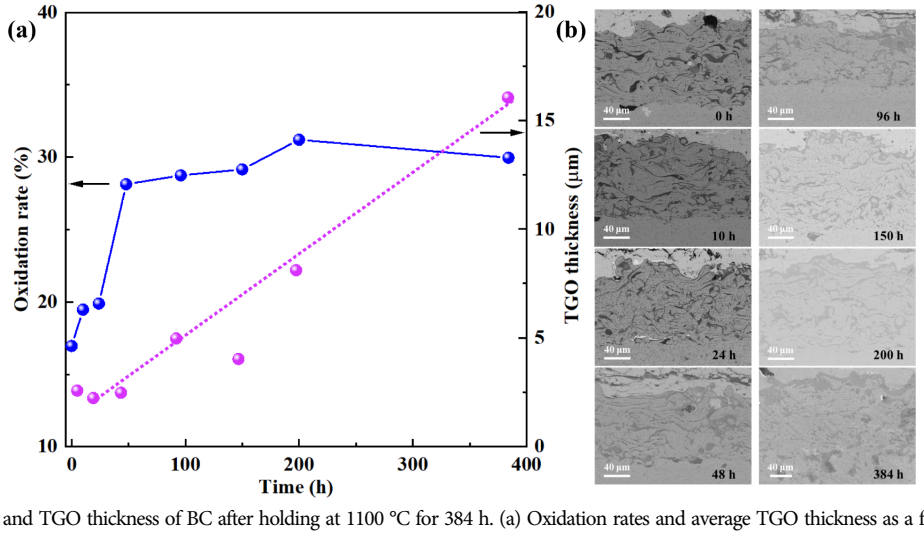


**Fig. 10** Oxidation rates and TGO thickness of BC after holding at 1100 °C for 384 h. (a) Oxidation rates and average TGO thickness as a function of holding time; (b) typical microstructures used to calculate oxidation rates and TGO thickness. Oxidation rates increase with increasing holding time, reaching a maximum (31.2%) after 200 h, and further oxidation is not triggered with prolonged holding time.

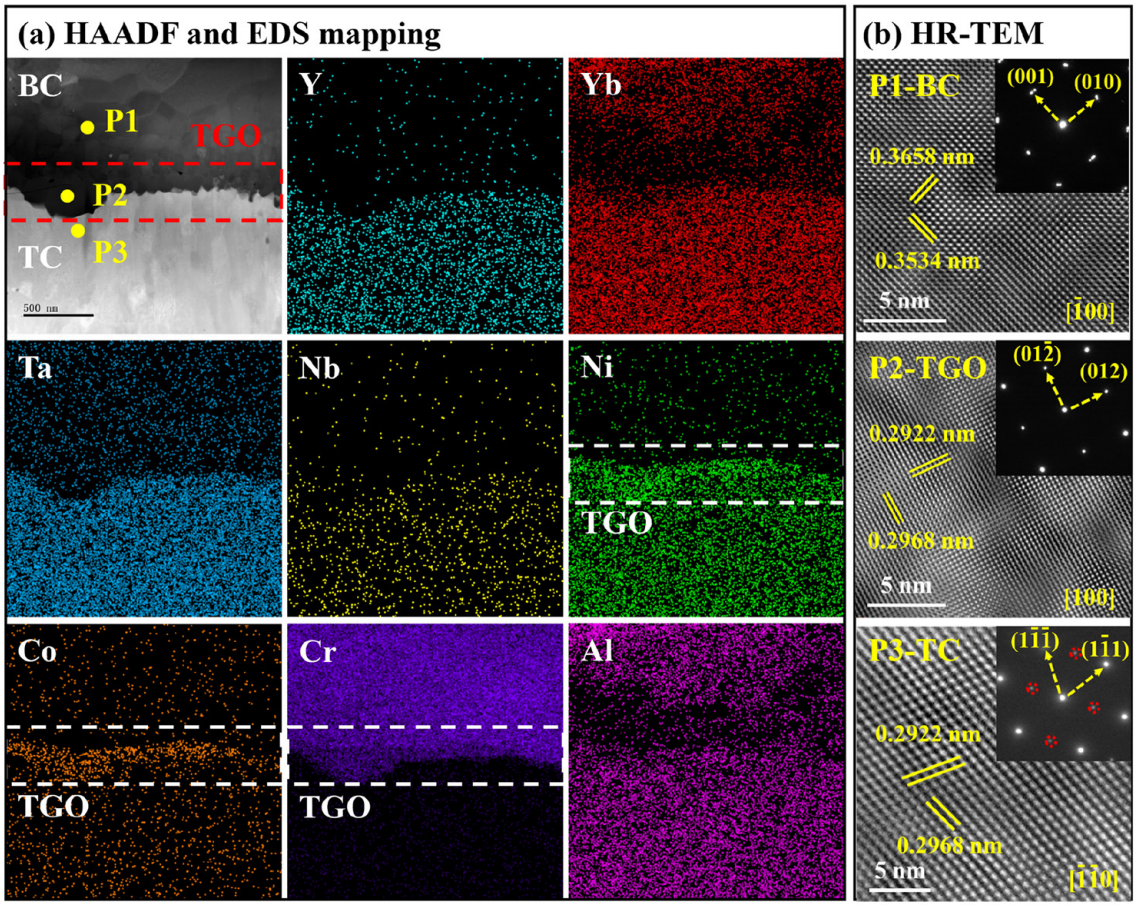


**Fig. 11** Typical interfacial structures and elemental distributions of tantalate HEC coatings after holding at 1100 °C for 200 h. (a) HAADF and EDS mapping; (b) high-resolution TEM (HR-TEM) and corresponding selected area electron diffraction (SAED) of different phases. BC is obviously oxidized to form $NiCr_2O_4$ TGO.

**Table 2** Elemental contents of P2 and P3 marked in Fig. 11

| Point | Al | Cr | Co | Ni | Y | Zr | Nb | Yb | Ta |
|---|---|---|---|---|---|---|---|---|---|
| P2 | 3.82 | 21.61 | 4.87 | 9.18 | 0.01 | 0.29 | 0.06 | 0.36 | 0.26 |
| P3 | 0.00 | 0.70 | 0.09 | 0.00 | 5.43 | 22.47 | 0.83 | 4.56 | 4.11 |

reduced due to high-temperature sintering and lead to increments in hardness and modulus. Meanwhile, the internal thermal stress increases with increasing holding time, which results in the production of cracks at the interface between the ceramic coatings and BC. Figure S10 in the ESM shows that obvious transverse cracks are found in the vicinity of BC, which reduce the hardness and toughness measured by Vickers's indentation. Figure 12(c) shows that the hardness reaches a maximum after holding at 1100 °C for 150 h, and Fig. 12(d) shows that the toughness (0.63–0.76 $MPa{\cdot}m^{1/2}$) is stable with increasing time. Table 3 lists the comprehensive mechanical properties of ceramic coatings, and the toughness is similar to that of 7YSZ coatings [2,10]. The high toughness inhibits the formation and propagation of cracks to increase the lifetime. The nanohardness is much higher than that measured by Vickers's hardness because nano-indentation can avoid the cracks and pores in coatings, as shown in Fig. S10 in the ESM.

The evolutions of hardness and modulus indicate that tantalate HEC coatings are stiffened after thermal measurements, which reduces the strain tolerance. At the same time, the pores and cracks are reduced in ceramic coatings, while thermal stress is increased at the interface between ceramic coatings and BC. Therefore, sintering and stiffening are harmful for tantalate HEC coatings. Considering that the changes in mechanical properties and stress are more rapid at higher cycling temperatures, the measuring times of thermal shock at 1500 °C are much less than those of thermal fatigue at 1150 °C.

### 4.3 Evolutions of thermal stress

Thermal stress leads to the failure of coatings, and different types of thermal stress exist in ceramic coatings and their interface [60]. The widely reported failure mechanisms of APS coatings under thermal measurements are shown in Figs. 13(a)–13(c) [2,10,61,62], and the interfacial thermal stress ($\sigma_N$) between BC and TGO is tensile in the undulation peak of TGO, while it is compressive in the undulation valley [2]. Figure 13(d) shows that ceramic coatings are subjected to radial stress ($\sigma^*$) [63]. The interfacial stress between BC and TGO results in interfacial cracks, and the inner stress in ceramic coatings leads to numerous tiny cracks. The cracks interlinking and coarsening will form a penetrating transverse crack, resulting in coating spalling, as observed in Figs. 6 and 7. Furthermore, other failure mechanisms are also observed in this work, including recrystallization and partial spalling of ceramic coatings [47,59], and TGO has a thickness larger than the critical thickness of 5–6 μm [2,54,55,64]. Therefore, the failure mechanisms of tantalate HEC coatings

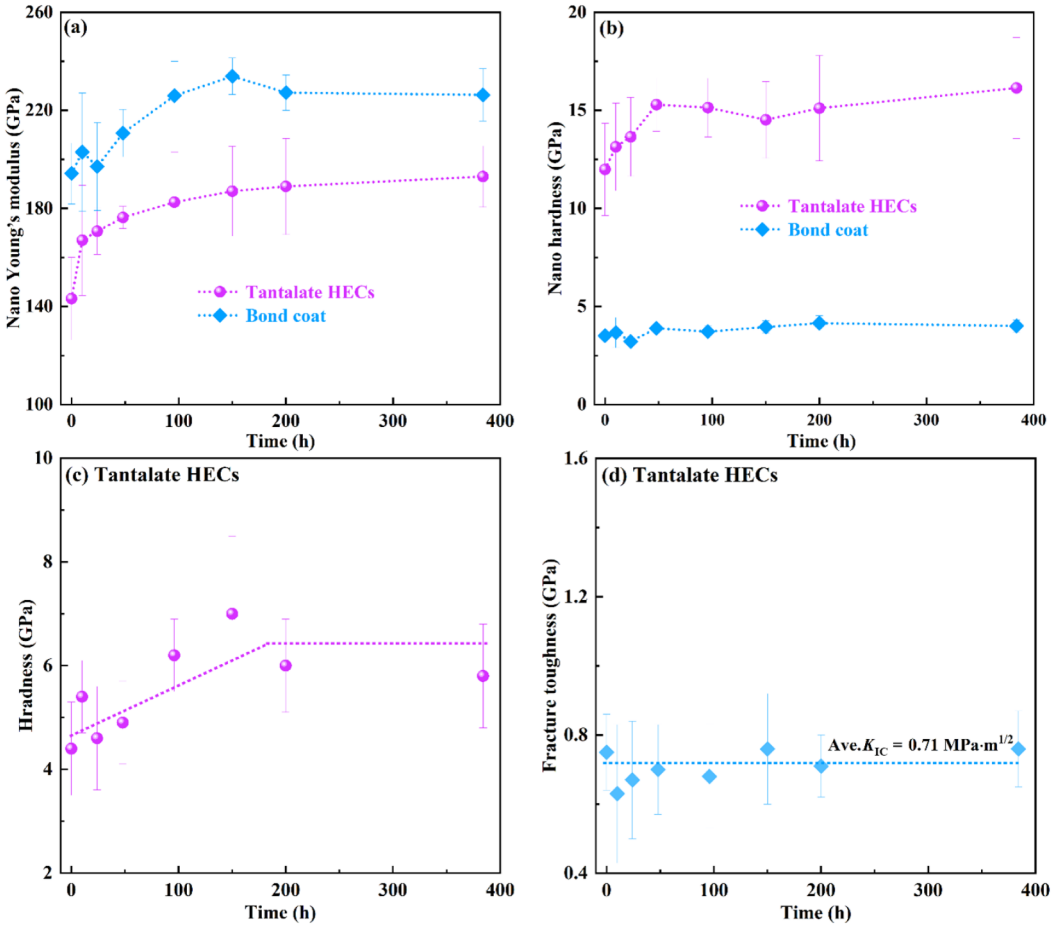


**Fig. 12** Mechanical properties of tantalate HEC coatings after holding at 1100 °C for 384 h. (a) Nano Young's modulus; (b) nanohardness; (c) Vickers hardness; (d) fracture toughness. Modulus, hardness, and toughness of tantalate HEC coatings are increased due to sintering and densification caused by heat treatments at 1100 °C. There are obvious differences in mechanical properties among tantalate HEC coatings, TGO, and substrates, which cause thermal stress.

**Table 3** Mechanical properties of tantalate HEC coatings, including hardness ($H_{nano}$ (GPa)) and Young's modulus ($E_{nano}$ (GPa)) measured via nano-indentation and hardness ($H$ (GPa)) and fracture toughness ($K_{IC}$ (MPa·m$^{1/2}$)) measured via Vickers indenter

| Time (h) | $H_{nano}$ (GPa) | $E_{nano}$ (GPa) | $H$ (GPa) | $K_{IC}$ (MPa·m$^{1/2}$) |
|---|---|---|---|---|
| 0 | 12.0±2.4 | 143.2±16.8 | 4.4±0.9 | 0.75±0.11 |
| 10 | 13.1±2.2 | 167.0±22.5 | 5.4±0.7 | 0.63±0.20 |
| 24 | 13.6±2.0 | 170.7±9.5 | 4.6±1.0 | 0.67±0.17 |
| 48 | 15.3±1.4 | 176.3±4.5 | 4.9±0.8 | 0.70±0.13 |
| 96 | 15.1±1.5 | 182.6±20.3 | 6.2±0.7 | 0.68±0.15 |
| 150 | 14.5±2.0 | 187.1±18.3 | 7.0±1.5 | 0.76±0.16 |
| 200 | 15.1±2.7 | 188.9±19.6 | 6.0±0.9 | 0.71±0.09 |
| 384 | 16.1±2.6 | 193.0±12.5 | 5.8±1.0 | 0.76±0.11 |

under differential thermal measurements are further analyzed.

During thermal shock at 1500 °C, the surface temperature of the ceramic coatings reaches 1500 °C, while the temperatures of the BC and substrate are much lower. Considering that Ni-based BC is severely oxidized at temperatures beyond 1075 °C [65] and the limit working temperature is 1150 °C, it is reasonable to assume that the temperature of BC is 1150 °C. Therefore, the temperature gradient ($\Delta T$) between ceramic coatings and BC is as high as 350 °C. The differences in TECs (ΔTECs) result in significant thermal stress ($\sigma$), which is calculated using Eq. (3) [58,66]:

$$\sigma = \frac{E}{1-\nu} \cdot \Delta T \cdot \Delta \mathrm{TECs} \tag{3}$$

where $E$ and $\nu$ are the Young's modulus and Poisson's ratio of tantalate HEC coatings, respectively. The thermal stress is proportional to the modulus, temperature gradient, and ΔTECs. BC (TECs = (16–18)×10$^{-6}$ K$^{-1}$) usually has much higher TECs than ceramic coatings (TECs = 11×10$^{-6}$ K$^{-1}$) [67,68], and enormous thermal stress (0.2–0.32 GPa) is induced.

However, the undulation TGO and its thickening result in thermal stress in ceramic coatings, as shown in Fig. 13(d). The radial stress ($\sigma^*$) in BC is tensile and related to ΔTECs between BC and ceramic coatings, which leads to hoop compressions in ceramic coatings. $\sigma^*$ is calculated according to Eq. (4) [61,63]:

$$\sigma^* = \frac{(\mathrm{TECs}_{comp} - \mathrm{TECs}_{ceramic})\,\Delta T'}{\frac{1-\nu_{ceramic}}{2E_{ceramic}} + \frac{1-2\nu_{comp}}{E_{comp}}} \tag{4}$$

where $\mathrm{TECs}_{comp}$ and $\mathrm{TECs}_{ceramic}$ are TECs of BC+TGO compounds and ceramic coatings, respectively; the subscript comp and ceramic represent BC+TGO compounds and ceramic coatings, respectively, for the modulus $E$ and Poisson's ratio $\nu$; $\Delta T'$ means the temperature ranges. The $\mathrm{TECs}_{comp}$ are determined according to Eqs. (5)–(7) [61,63]:

$$\mathrm{TECs}_{comp} = \mathrm{TECs}_{TGO} + \frac{P_3(\mathrm{TECs}_{BC} - \mathrm{TECs}_{TGO})}{P_2} \tag{5}$$

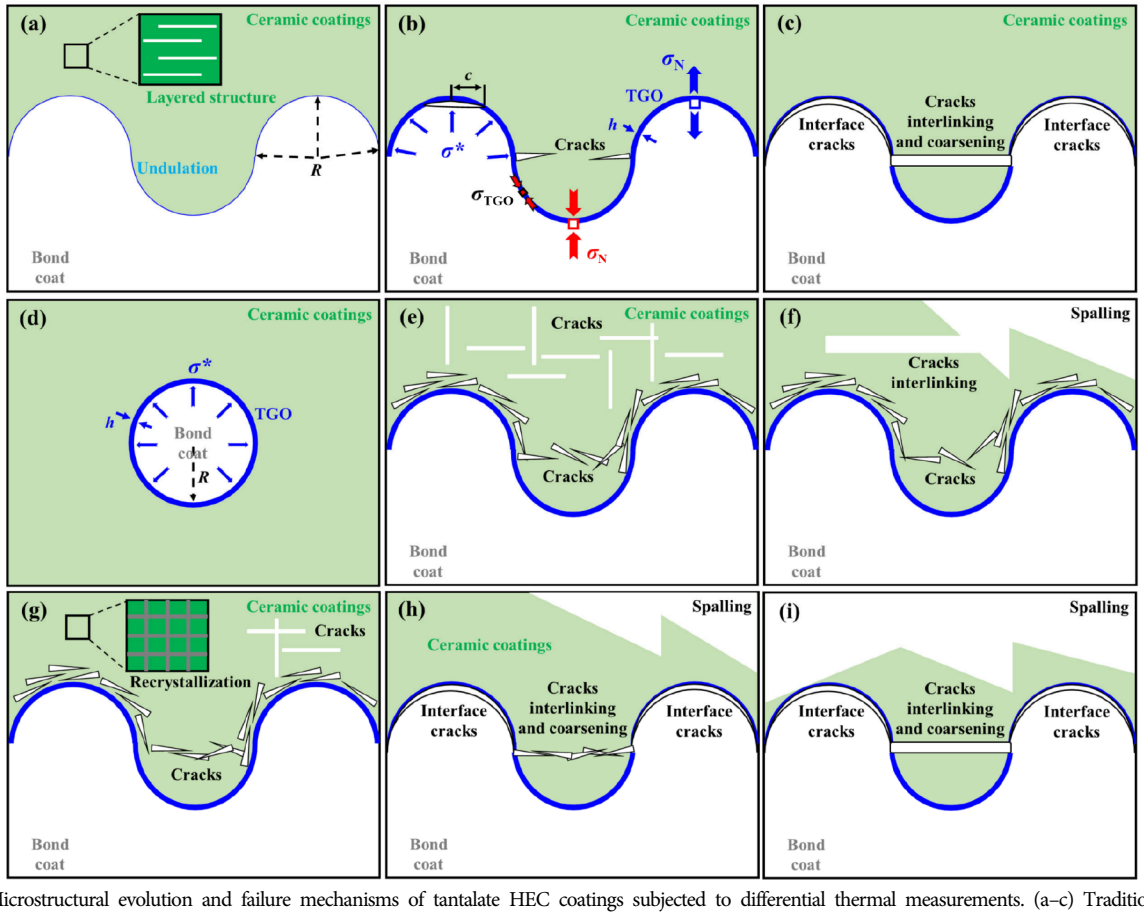


**Fig. 13** Microstructural evolution and failure mechanisms of tantalate HEC coatings subjected to differential thermal measurements. (a–c) Traditional failure mechanisms of TBCs reported in other works [2,10]; (d) sketch map of estimations for internal thermal stress of ceramic coatings; (e, f) failure mechanisms of tantalate HEC coatings subjected to thermal shock at 1500 °C; (g–i) failure mechanisms of tantalate HEC coatings subjected to thermal fatigue at 1150 °C.

$$P_2 = \frac{R^3(1+\nu_{TGO}) + 2(R-h)^3(1-2\nu_{TGO})}{2R^3 - 2(R-h)^3} + \frac{E_{TGO}(1-2\nu_{BC})}{E_{BC}} \tag{6}$$

$$P_3 = \frac{3R^3(1-\nu_{TGO})}{2R^3 - 2(R-h)^3} \tag{7}$$

where $h$ and $R$ are the thickness and radius of the TGO undulation, respectively, as shown in Fig. 13(b). Therefore, the ceramic coatings are subjected to two types of thermal stress, and they are cracked when the stress intensity factor ($K$) around the cracks is higher than the fracture toughness of the ceramic coatings. $K$ is calculated according to Eq. (8) [64,69]:

$$K^* = \lambda \cdot \sigma^* \sqrt{\frac{\pi \cdot R}{2}\left(\frac{c}{R} - 1\right)} \cdot \left(\frac{R}{c}\right)^{2.4} \tag{8}$$

where $\lambda$ = 2.5–3.0 is a factor relating to the elastic misfits between BC and TGO, and $c$ is the crack radius [69]. $K^*$ is affected by the $h/R$ ratio. $K^*$ first increases with the $c/R$ ratio and then decreases when the $h/R$ ratio is constant. Figure 14(a) shows that $K^*$ is less than the average fracture toughness (Ave.$K_{IC}$ = 0.71 MPa·m$^{1/2}$) of ceramic coatings when $\lambda$ is set as 2.5. The $h/R$ = 0.10–0.71 is obtained from Fig. 10, while $h/R$ = 1.00 and 2.00 are set to further estimate the evolution of the stress intensity factor. Figure 14(b) shows that $K^*$ is higher than Ave.$K_{IC}$ when $h/R$ is higher than 0.32, i.e., the holding time at 1100 °C reaches 200 h, and $\lambda$ is set as 3.0. The ceramic coatings will not fracture when $K^*$ is less than Ave.$K_{IC}$, and two intersections are found between the Ave.$K_{IC}$ line and stress intensity factor when $h/R$ is 0.71–2.00. The first intersection ($c_0/R$) means that the cracks are formed and propagated in ceramic coatings, and the second intersection ($c^*/R$) means that the neighboring cracks in the adjacent undulation peaks coalesce to further promote their enlargements and propagations.

Obviously, the $h/R$ ratio during thermal shock at 1500 °C is far less than 0.32, as shown in Figs. 5 and 6; however, obvious transverse cracks are found, which are different from the above discussion. Namely, the cracks and their interlinkages should not occur when only the hoop stress is considered. Additionally, the spalling of tantalate HEC coatings begins at the center of the sample, meaning that the effects of thermal stress caused by the temperature gradient are significant. Accordingly, cracks are produced in the tantalate HEC coatings under the joint effects of hoop stress and temperature gradient stress, and temperature gradient stress plays a major role during thermal shock at 1500 °C. The failure mechanisms of tantalate HEC coatings are shown in Figs. 13(e) and 13(f), i.e., numerous tiny cracks are formed in ceramic coatings under the effects of hoop stress and temperature gradient stress, and these cracks coalesce to form transverse cracks, which lead to spalling of coatings. These cracks mainly propagate in ceramic coatings, as a stiff TGO layer is not yet formed, and the toughness of the TGO layer is usually higher than that of porous ceramic coatings. The strain energy release rate during crack deflection along the TGO/TC interface is approximately twice that during crack propagation toward the TGO/BC interface [2,69]. Thus, most cracks exist in tantalate HEC coatings, and they do not propagate into the TGO, which is consistent with the microstructures shown in Fig. 5(b).

The ceramic coating spalling and failure mechanisms of

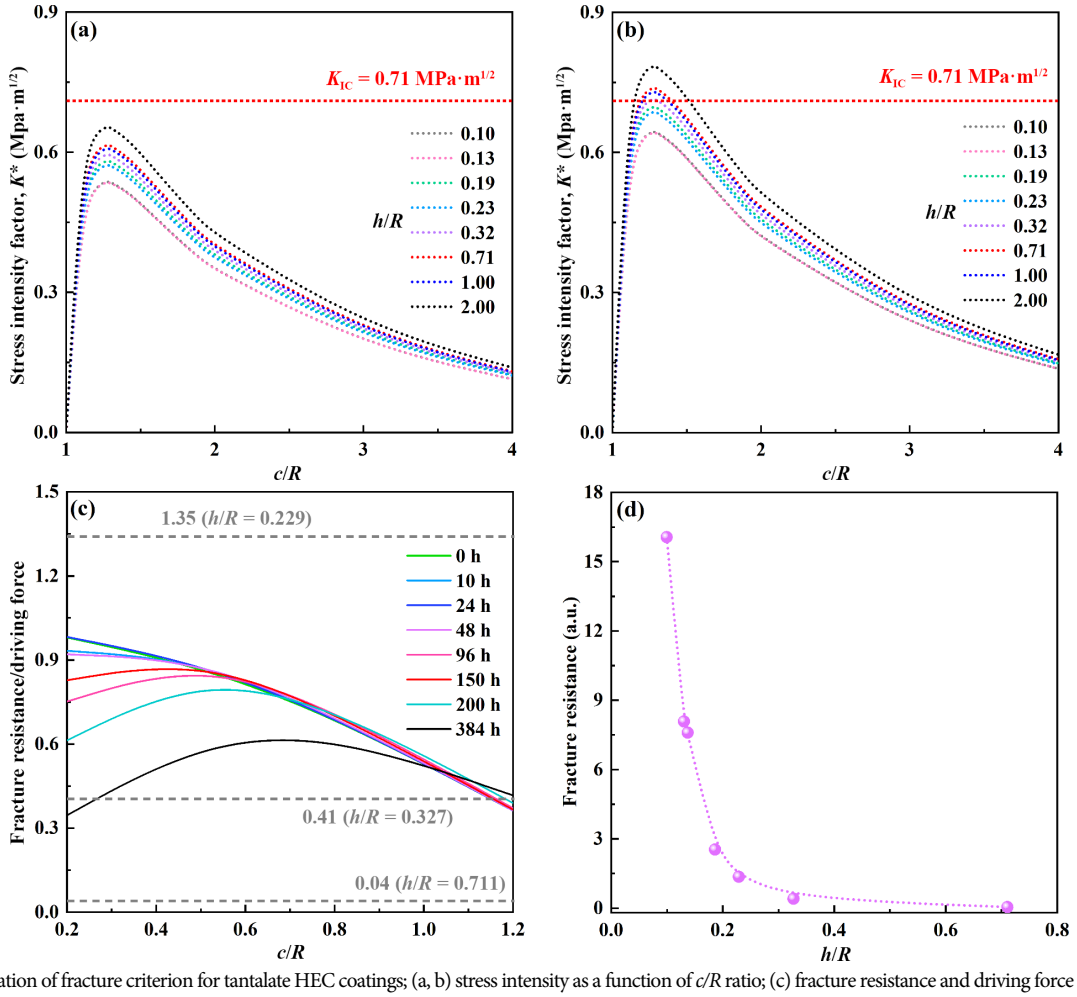


**Fig. 14** Estimation of fracture criterion for tantalate HEC coatings; (a, b) stress intensity as a function of *c*/*R* ratio; (c) fracture resistance and driving force as a function of *c*/*R* ratio; (d) fracture resistance as a function of *h*/*R*. Stress intensity factor is proportional to *h*/*R* ratio, and increasing TGO thickness will increase stress intensity factor to cause failure of tantalate HEC coatings. Furthermore, driving force is higher than fracture resistance when *h*/*R* is higher than 0.32, proving that formation and propagation of TGO are dominant factors for coating failure.

thermal fatigue are different from those of thermal shock, and the TGO/BC interface is cracked when the inner thermal stress is higher than the critical values. The criterion for interfacial fracture is given by Eq. (9) [10]:

$$\frac{\pi \cdot R^2 \cdot E_{\mathrm{TGO}} \cdot \Gamma}{2B \cdot h^3 \cdot \sigma_{\mathrm{TGO}}^2} \leq \left[ \left(1 - \mathrm{e}^{-\frac{c}{h}}\right) \cos\frac{c}{R} + \mathrm{e}^{-c/h} \frac{R}{2h} \sin\frac{c}{R} \right] \quad (9)$$

where $\sigma_{\mathrm{TGO}}$ and $E_{\mathrm{TGO}}$ are the inner thermal stress and modulus of TGO undulation, respectively; $\Gamma$ is the fracture energy of the TGO/BC interface; $B$ is a constant on the order of unity. The left side of Eq. (9) represents the fracture resistance, and the other side represents the driving force. $E_{\mathrm{TGO}}$, $R$, $h$, and $\sigma_{\mathrm{TGO}}$ have essential effects on the fracture resistance of the TGO/BC interface. The thermal stress ($\sigma_{\mathrm{N}}$) acting on the BC/TGO interface is estimated under the assumptions that the ceramic coatings have no influence and that there is no layering in the TGO. It is calculated according to Eq. (10) [2,10]:

$$\sigma_{\mathrm{N}} = \frac{2\sigma_{\mathrm{TGO}} \cdot h}{R} \quad (10)$$

where $\sigma_{\mathrm{TGO}}$ is approximately 1–2 GPa [10], and $\sigma_{\mathrm{N}}$ is approximately 0.20–2.84 GPa based on the changes in TGO thickness.

Figure 14(c) shows that the TGO/BC interface is cracked when the *h*/*R* ratio is higher than 0.32, and the TGO thickness is approximately 8.1 μm after holding at 1100 °C for 200 h. In Fig. 14(c), the gray dashed lines are fracture resistance, and it decreases dramatically with increasing *h*/*R* ratio. The left intersection point between fracture resistance and driving force means that the TGO/BC interface is cracked, while the right intersection point means that different cracks are interconnected, as shown in Fig. 13(d). Crack interlinking and coarsening lead to interfacial spalling of tantalate HEC coatings, and recrystallization and enhanced coating stiffness result in surficial coating spalling. Figure 14(d) shows that the fracture resistance decreases sharply with increasing *h*/*R* ratio, meaning that the desired driving force for coating spalling is reduced with increasing TGO thickness. Accordingly, two-type modes of coating spalling are found in Fig. 7 during thermal fatigue at 1150 °C. The TGO/BC interface is cracked due to the cumulative driving force caused by the increasing TGO thickness, while surficial coating spalling is caused by recrystallization and enhanced coating stiffness.

## 5 Conclusions

The designed and synthesized tantalate HEC coatings can work at temperatures up to 1500 °C, and they withstand thermal fatigue at 1150 °C for 12,830 cycles and thermal shock at 1500 °C for 614 cycles. Annealing at 1100 °C for 384 h is used to uncover the failure mechanisms of tantalate HEC coatings during different thermal measurements based on the evolution of the microstructure and TGO. During thermal shock at 1500 °C, the significant thermal gradient and the differences in TECs and

mechanical properties between BC and ceramic coatings produce enormous thermal stress, which leads to the failure of tantalate HEC coatings. Additionally, sintering recrystallization and increasing stiffness result in surficial layered peeling of ceramic coatings. The oxidation rate of BC and thickness of TGO dominate the failure mechanisms of tantalate HEC coatings during thermal fatigue at 1150 °C, and the driving force of cracks is higher than the fracture resistance when $h/R$ is beyond 0.32, which responds to the final failure of ceramic coatings. Accordingly, the TGO thickness $h$ and thermal stress caused by the thermal gradient and the differences in TECs and mechanical properties between BC and ceramic coatings are the dominators for the failure of tantalate HEC coatings in this work. The current coatings have a thickness of approximately 150 μm, which is thinner than the typical TBCs (250–400 μm) used in gas turbine applications. Considering that tantalate HECs possess a low thermal conductivity, which is lower than that of conventional YSZ, the thermal insulation performance can be further enhanced by increasing the coating thickness. For moderate-temperature applications (1100–1300 °C) such as stationary gas turbines, the current 150 μm coatings may provide sufficient thermal protection, while for ultrahigh-temperature applications (1400–1500 °C) such as aero-engine turbine blades, increasing the thickness to 300–400 μm would provide a larger temperature drop and better protect the substrates. Future research should focus on optimizing APS parameters to achieve thicker coatings and establishing quantitative relationships between coating thickness, thermal gradient, and service life, which will further promote the applications of tantalate HECs as next-generation high-performance TBCs.

## Acknowledgements

We greatly appreciate the support from the National Natural Science Foundation of China (Nos. 52502065 and 52562006), Yunnan Major Scientific and Technological Project (No. 202302AG050010), Yunnan Province Innovation Team (No. 202305AS350018), and the Research Innovation Cultivation Project of Yunnan Province (No. FWCY-BSPY2024051).

## Author contributions

Jiankun Wang: investigation, writing–original draft preparation; Lin Chen: methodology, resources, writing–review and editing, supervision; Luyang Zhang: methodology, analysis; Hao Xu: investigation, analysis; Qinglin Zhou: analysis; Jing Feng: conceptualization, resources, writing–review and editing, supervision.

## Availability of data and materials

The data that support the findings of this study are available from the corresponding author upon reasonable request.

## Competing interests

The authors have no competing interests to declare that are relevant to the content of this article. The author Jing Feng is the Editorial Committee member of this journal.

## Electronic Supplementary Material

Supplementary material is available in the online version of this article at https://doi.org/10.26599/JAC.2026.9221261.

## References

[1] Padture NP. Advanced structural ceramics in aerospace propulsion. *Nat Mater* 2016, **15**: 804–809.

[2] Schlichting KW, Padture NP, Jordan EH, *et al.* Failure modes in plasma-sprayed thermal barrier coatings. *Mat Sci Eng A—Struct* 2003, **342**: 120–130.

[3] Chen L, Li BH, Feng J. Rare-earth tantalates for next-generation thermal barrier coatings. *Prog Mater Sci* 2024, **144**: 101265.

[4] Sternlicht H, McComb DW, Padture NP. Interaction of ytterbium pyrosilicate environmental-barrier-coating ceramics with molten calcia–magnesia–aluminosilicate glass: Part II, Interfaces. *Acta Mater* 2022, **241**: 118359.

[5] Zhang S, Zhang J, Wang XH, *et al.* Preparation, mechanical, and thermal properties of $CrNbO_4$: A novel dual-functional scale to protect RHEAs from oxidation and thermal attack. *J Adv Ceram* 2025, **14**: 9221100.

[6] Chevalier J, Gremillard L, Virkar AV, *et al.* The tetragonal–monoclinic transformation in zirconia: Lessons learned and future trends. *J Am Ceram Soc* 2009, **92**: 1901–1920.

[7] Chen L, Hu MY, Zheng XD, *et al.* Characteristics of ferroelastic domains and thermal transport limits in $HfO_2$ alloying $YTaO_4$ ceramics. *Acta Mater* 2023, **251**: 118870.

[8] Liu Y, Zhuang L, Xie PB, *et al.* $(Gd_{1/7}Dy_{1/7}Ho_{1/7}Er_{1/7}Tm_{1/7}Yb_{1/7}Lu_{1/7})_2Si_2O_7$ high-entropy disilicate: A promising environmental barrier coating material. *Sci China Mater* 2024, **67**: 2694–2699.

[9] Wright AJ, Wang QY, Yeh YT, *et al.* Short-range order and origin of the low thermal conductivity in compositionally complex rare-earth niobates and tantalates. *Acta Mater* 2022, **235**: 118056.

[10] Clarke DR, Pompe W. Critical radius for interface separation of a compressively stressed film from a rough surface. *Acta Mater* 1999, **47**: 1749–1756.

[11] Chen L, Hu MY, Wang JK, *et al.* Dominant mechanisms of thermo–mechanical properties of weberite-type $RE_3TaO_7$ (RE = La, Pr, Nd, Eu, Gd, Dy) tantalates toward multifunctional thermal/environmental barrier coating applications. *Acta Mater* 2024, **270**: 119857.

[12] Scotson D, Paksoy AH, Xiao P. Characterisation techniques for investigating TBC and EBC failure: A review. *Front Ceram* 2024, **1**: 1307437.

[13] Han Y, Liu XY, Zhang QQ, *et al.* Ultra-dense dislocations stabilized in high entropy oxide ceramics. *Nat Commun* 2022, **13**: 2871.

[14] Li BH, Wang JK, Chen L, *et al.* Breaking the trade-off relationship between thermal conductivity and toughness of ferroelastic oxide ceramics via a high-density dislocation strategy. *Adv Mater* 2026, **38**: 23083.

[15] Huang L, Liu MJ, Yang GJ, *et al.* Treelike PS-PVD coating: Hierarchical branching by shading and sintering. *Acta Mater* 2024, **280**: 120321.

[16] Yu ZY, Wei LL, Guo XY, *et al.* Microstructural evolution, mechanical properties and degradation mechanism of PS-PVD quasi-columnar thermal barrier coatings exposed to glassy CMAS deposits. *Rare Metals* 2024, **43**: 3329–3340.

[17] Chen L, Luo KR, Li BH, *et al.* Mechanical property enhancements and amorphous thermal transports of ordered weberite-type $RE_3Nb/TaO_7$ high-entropy oxides. *J Adv Ceram* 2023, **12**: 399–413.

[18] Wang JK, Chen L, Li BH, *et al.* Evolutions of mechanical and thermal properties of $TmNbO_4/Tm_3NbO_7$ composites as protective coating materials. *J Adv Ceram* 2024, **13**: 1771–1785.

[19] Cao XQ, Vassen R, Wang JS, *et al.* Degradation of zirconia in moisture. *Corros Sci* 2020, **176**: 109038.

[20] Zhang DW, Chen Y, Vega H, *et al.* Long- and short-range orders in 10-component compositionally complex ceramics. *Adv Powder Mater* 2023, **2**: 100098.

[21] Li YR, Pan DH, Cao JH, *et al.* Recent advances in high-entropy ceramics: Design principles, structural characteristics, and emerging properties. *Extreme Mater* 2025, **1**: 42–72.

[22] Chen L, Wang YT, Hu MY, *et al.* Achieved limit thermal conductivity and enhancements of mechanical properties in fluorite $RE_3NbO_7$ via entropy engineering. *Appl Phys Lett* 2021, **118**: 071905.

[23] Akrami S, Edalati P, Fuji M, *et al.* High-entropy ceramics: Review of principles, production and applications. *Mat Sci Eng R* 2021, **146**: 100644.

[24] Fan Y, Bai YL, Lu ZY, *et al.* Exploring high-performance environmental barrier coatings for rare earth silicates: A combined

approach of first principles calculations and machine learning. *J Materiomics* 2025, **11**: 100921.
[25] Gan MD, Lai LP, Wang JK, *et al.* Suppressing the oxygen-ionic conductivity and promoting the phase stability of the high-entropy rare earth niobates via Ta substitution. *J Mater Sci Technol* 2025, **209**: 79–94.
[26] Sun LC, Luo YX, Tian ZL, *et al.* High temperature corrosion of $(Er_{0.25}Tm_{0.25}Yb_{0.25}Lu_{0.25})_2Si_2O_7$ environmental barrier coating material subjected to water vapor and molten calcium–magnesium–aluminosilicate (CMAS). *Corros Sci* 2020, **175**: 108881.
[27] Zhuang L, Wen ZH, Liu YW, *et al.* Unveiling the oxidation mechanisms of high-entropy carbides through atomic-scale dynamic observation. *Adv Mater* 2025, **37**: 2417846.
[28] Wang Z, Yuan MK, Gao JT, *et al.* Effective suppression of surface cation segregations on double perovskite oxides through entropy engineering. *J Rare Earth* 2025, **43**: 345–353.
[29] Xue GY, Wang JK, Li CY, *et al.* High-entropy effects enhance atomic displacements to manipulate thermal/oxygen ionic transport properties of ordered $RE_3MO_7$ ceramics. *Rare Metals* 2025, **44**: 10660–10671.
[30] Chen YF, Hong CQ, Hu CL, *et al.* Ceramic-based thermal protection materials for aerospace vehicles. *Adv Ceram* 2017, **38**: 311–390. (in Chinese)
[31] Raghavan S, Wang H, Dinwiddie RB, *et al.* $Ta_2O_5/Nb_2O_5$ and $Y_2O_3$ co-doped zirconias for thermal barrier coatings. *J Am Ceram Soc* 2004, **87**: 431–437.
[32] Gurak M, Flamant Q, Laversenne L, *et al.* On the yttrium tantalate–zirconia phase diagram. *J Eur Ceram Soc* 2018, **38**: 3317–3324.
[33] Wang JK, Chen L, Wang G, *et al.* Dual-phase zirconate/tantalate high-entropy ceramics boost thermal properties and fracture toughness for thermal barrier coating materials. *J Mater Res Technol* 2024, **32**: 3825–3830.
[34] Chen XL, Chen L, Tian J, *et al.* Measurements and applications of thermal-mechanical properties of thermal/environmental barrier coating materials. *Adv Ceram* 2025, **46**: 389–415. (in Chinese)
[35] Ponton CB, Rawlings RD. Vickers indentation fracture toughness test Part 2 Application and critical evaluation of standardised indentation toughness equations. *Mater Sci Tech-Lond* 1989, **5**: 961–976.
[36] Shen Y, Clarke DR. Resistance to low-temperature degradation of equimolar $YO_{1.5}$–$TaO_{2.5}$ stabilized tetragonal $ZrO_2$ ceramics in air. *J Am Ceram Soc* 2010, **93**: 2024–2027.
[37] Van Sluytman JS, Krämer S, Tolpygo VK, *et al.* Microstructure evolution of $ZrO_2$–$YbTaO_4$ thermal barrier coatings. *Acta Mater* 2015, **96**: 133–142.
[38] Li P, Chen IW, Penner-Hahn JE. Effect of dopants on zirconia stabilization—An X-ray absorption study: III, charge-compensating dopants. *J Am Ceram Soc* 1994, **77**: 1289–1295.
[39] Wang L, Yang JS, Ni JX, *et al.* Influence of cracks in APS–TBCs on stress around TGO during thermal cycling: A numerical simulation study. *Surf Coat Tech* 2016, **285**: 98–112.
[40] Zhang YJ, Zou H, You XM, *et al.* Study on influence of different plasma gas ratio on PS-PVD jet and coating structure. *J Therm Spray Techn* 2024, **16**: 55–64. (in Chinese)
[41] Sezavar A, Sajjadi SA. A review on the performance and lifetime improvement of thermal barrier coatings. *J Eur Ceram Soc* 2025, **45**: 117274.
[42] Chen L, Li SW, Li CJ, *et al.* Reactive self-consumption strategy to suppress $SiO_2$ phase transition-induced cracking. *J Adv Ceram* 2025, **14**: 9221042.
[43] Huang AH, Li L, Liu XZ, *et al.* Phase transformation-induced TGO rumpling failure of an AlCoCrFeNi high-entropy alloy after isothermal oxidation at 1200 °C. *Scripta Mater* 2024, **239**: 115817.
[44] Dong H, Liang XH, Bai JC, *et al.* The relationship between the film hole distribution and thermal cycle performance of TBCs by APS and HVOF. *Surf Coat Tech* 2023, **467**: 129694.
[45] Dong H, Yang GJ, Li CX, *et al.* Effect of TGO thickness on thermal cyclic lifetime and failure mode of plasma-sprayed TBCs. *J Am Ceram Soc* 2014, **97**: 1226–1232.
[46] Liang GY, Zhu C, Wu XY, *et al.* The formation model of Ni–Cr oxides on NiCoCrAlY-sprayed coating. *Appl Surf Sci* 2011, **257**: 6468–6473.
[47] Cheng B, Zhang YM, Yang N, *et al.* Sintering-induced delamination of thermal barrier coatings by gradient thermal cyclic test. *J Am Ceram Soc* 2017, **100**: 1820–1830.
[48] Zhang BY, Yang GJ, Li CX, *et al.* Non-parabolic isothermal oxidation kinetics of low pressure plasma sprayed MCrAlY bond coat. *Appl Surf Sci* 2017, **406**: 99–109.
[49] Karaoglanli AC, Turk A. Isothermal oxidation behavior and kinetics of thermal barrier coatings produced by cold gas dynamic spray technique. *Surf Coat Tech* 2017, **318**: 72–81.
[50] Chen WR, Wu X, Marple BR, *et al.* TGO growth behaviour in TBCs with APS and HVOF bond coats. *Surf Coat Tech* 2008, **202**: 2677–2683.
[51] Toscano J, Vaβen R, Gil A, *et al.* Parameters affecting TGO growth and adherence on MCrAlY-bond coats for TBC's. *Surf Coat Tech* 2006, **201**: 3906–3910.
[52] Hille TS, Turteltaub S, Suiker ASJ. Oxide growth and damage evolution in thermal barrier coatings. *Eng Fract Mech* 2011, **78**: 2139–2152.
[53] Che C, Wu GQ, Qi HY, *et al.* Uneven growth of thermally grown oxide and stress distribution in plasma-sprayed thermal barrier coatings. *Surf Coat Tech* 2009, **203**: 3088–3091.
[54] Zhang BY, Meng GH, Yang GJ, *et al.* Dependence of scale thickness on the breaking behavior of the initial oxide on plasma spray bond coat surface during vacuum pre-treatment. *Appl Surf Sci* 2017, **397**: 125–132.
[55] Rabiei A, Evans AG. Failure mechanisms associated with the thermally grown oxide in plasma-sprayed thermal barrier coatings. *Acta Mater* 2000, **48**: 3963–3976.
[56] Pei HQ, Li M, Wang P, *et al.* The effect of tensile stress on oxidation behavior of nickel-base single crystal superalloy. *Corros Sci* 2021, **191**: 109737.
[57] Xu QL, Liu KC, Wang KY, *et al.* TGO and Al diffusion behavior of $CuAl_xNiCrFe$ high-entropy alloys fabricated by high-speed laser cladding for TBC bond coats. *Corros Sci* 2021, **192**: 109781.
[58] Busso EP, Qian ZQ, Taylor MP, *et al.* The influence of bondcoat and topcoat mechanical properties on stress development in thermal barrier coating systems. *Acta Mater* 2009, **57**: 2349–2361.
[59] Li GR, Liu T, Luo XT, *et al.* Tailoring sintering-resistant thermal barrier coatings by considering critical healing width of two-dimensional interlamellar pores. *J Adv Ceram* 2023, **12**: 1317–1330.
[60] Li JM, Li S, Shi J, *et al.* The failure behavior analysis based on finite element simulation of PS-PVD $(Gd_{0.9}Yb_{0.1})_2Zr_2O_7$/YSZ coatings during burner rig tests. *Mater Design* 2023, **231**: 112013.
[61] Hsueh CH, Fuller ER. Analytical modeling of oxide thickness effects on residual stresses in thermal barrier coatings. *Scripta Mater* 2000, **42**: 781–787.
[62] Evans AG, Hutchinson JW. The mechanics of coating delamination in thermal gradients. *Surf Coat Tech* 2007, **201**: 7905–7916.
[63] Davidge RW. *Mechanical Behaviour of Ceramics*. London (UK): Cambridge University Press, 1979.
[64] Evans AG, He MY, Hutchinson JW. Mechanics-based scaling laws for the durability of thermal barrier coatings. *Prog Mater Sci* 2001, **46**: 249–271.
[65] Patil SM, Kumar KC, Radhakrishnan M, *et al.* Effect of heating rates on non-isothermal and isothermal oxidation behavior of additive friction stir deposited nickel base superalloy IN625. *Corros Sci* 2025, **256**: 113174.
[66] Martena M, Botto D, Fino P, *et al.* Modelling of TBC system failure: Stress distribution as a function of TGO thickness and thermal expansion mismatch. *Eng Fail Anal* 2006, **13**: 409–426.
[67] Monroe JA, Gehring D, Karaman I, *et al.* Tailored thermal expansion alloys. *Acta Mater* 2016, **102**: 333–341.
[68] Zhang LY, Chen L, Wang JK, *et al.* High entropy engineering boosts thermo-mechanical properties of rare-earth tantalates: Influences of cocktail effects. *J Materiomics* 2025, **11**: 100984.
[69] Shum DKM, Huang YY. Fundamental solutions for microcracking induced by residual stress. *Eng Fract Mech* 1990, **37**: 107–117.